Journal of Inorganic and Organometallic Polymers and Materials (2025) 35:2257–2273
https://doi.org/10.1007/s10904-024-03163-8

RESEARCH

Copper-Based Metal–Organic Framework: Synthesis, Characterization and Evaluation for the Hydrogenation of Furfural to Furfuryl Alcohol

Pamela S. Moyo[1] · Gift Mehlana[2] · Leah C. Matsinha[1] · Banothile C. E. Makhubela[1]

Received: 12 July 2023 / Accepted: 23 May 2024 / Published online: 7 October 2024

Abstract

A novel **Cu-MOF** was synthesized at room temperature from commercially available and inexpensive reagents. The pre-catalyst was characterized using X-ray photoelectron spectroscopy, high-resolution transmission electron microscopy, inductively coupled plasma-optical emission spectroscopy, Fourier transform-infrared spectroscopy, powder X-ray diffraction, Brunauer-Emmet-Teller (BET) and scanning electron microscopy-energy dispersive X-ray spectroscopy. The **Cu-MOF** was characterized as microporous material with BET surface area and pore volume of 7.47 m^2/g and 0.27 cm^3/g, respectively, and is stable in most solvents. The MOF was evaluated as a heterogeneous catalyst for the hydrogenation of furfural to furfuryl alcohol (FA). **Cu-MOF** exhibited a high conversion of FF (76%) with selectivity towards FA (100%) at 140 °C, 50 bar for 24 h. The MOF was reused four consecutive times with a loss in catalytic performance. The decrease in catalytic activity could be attributed to the formation of inactive Cu(0) as revealed by HR-TEM and XPS studies. The HR-TEM of spent **Cu-MOF** showed a uniform particle size diameter of 3.5 nm. This work is significant in providing new strategies for the design and fabrication of highly selective MOF catalysts for the FF upgrading.

Keywords Metal–organic framework · Heterogeneous catalyst · Furfural upgrading · Furfuryl alcohol

1 Introduction

Efforts are being made to minimize the negative environmental impact caused by using fossil fuels, such as coal, natural gas and petroleum, that often emit gases [like SOx, PFAS (per-and polyfluoroalkyl substances) and NOx] during processing [1, 2]. Lignocellulosic biomass has emerged as a viable substitution for fossil fuels in addressing these environmental concerns. It is found in plants and consists of cellulose, lignin and hemicellulose [3]. Hemicellulose can be depolymerized to produce xylose through hydrolysis using an acid catalyst. Several strategies for converting xylose into FF using both homogenous and heterogeneous catalysts have been extensively explored in the published literature [4, 5].

In 1921, industrial production of furfural (FF) was established by Quaker Oats technology [6]. FF is produced from oats hulls by employing high pressure, temperature and H_2SO_4 in a batch mode [7]. However, drawbacks such as high maintenance costs and low yield suggest that the reaction conditions must be optimized. China is the major producer and exporter of FF and furfuryl alcohol (FA) from corncobs [8]. South Africa is the third largest producer of FF from sugarcane bagasse and the production plant is owned by Illovo Sugar in Durban. Sappi in South Africa has also developed technology for the production of FF using hemicellulose extracted from the Pulp and Paper Mill in Ngodwana, outside of Mbombela. The U.S. Department of Energy, listed FF as one of the top 30 building blocks in 2004 [9]. FF can be further converted into useful downstream products such as furfuryl alcohol (FA), furan, tetrahydrofurfuryl alcohol (THFA), 2-methylfuran (MF),

✉ Gift Mehlana
mehlanag@staff.msu.ac.zw

✉ Leah C. Matsinha
leahmatsinha@gmail.com

✉ Banothile C. E. Makhubela
bmakhubela@uj.ac.za

Pamela S. Moyo
suzzanamoyo@gmail.com

[1] Research Centre for Synthesis and Catalysis, Department of Chemical Sciences, University of Johannesburg, Auckland Park, Johannesburg 2006, South Africa

[2] Department of Chemical Sciences, Midlands State University, 9055 Senga Road, Gweru, Zimbabwe

tetrahydrofuran (THF) and cyclopentanone and ring-opened products such as ethyl levulinate (EL), levulinic acid (LA), pentanediols (Fig. 1). FA is an important chemical intermediate for the production of chemical products, such as lysine, lubricant, aroma fragrance, plasticizer, dispersing agents, perfumes, resins and so on [10].

It is claimed that 62% of the total FF manufactured worldwide each year is processed into FA. FF is currently hydrogenated commercially in the vapour or liquid phase over a Cu-Cr catalyst [4, 5]. However, the severe and extensive impact of using chromium-based catalyst on human health and the environment has paved the way for exploring new catalysts. Cu-based catalysts are often employed for FF hydrogenation because of their excellent catalytic performance [11]. Various Cu-based catalysts such as Cu/TiO_2 and Cu/SiO_2 have been reported in the literature [12, 13]. Furthermore, metal–organic frameworks (MOFs) have been utilized for FF hydrogenation due to their unique characteristics such as chemical stability, tenability and high porosity [14]. Co/Cu MOF-74, $Cu/CuFe_2O_4$@C, Cu-BTCNi@C and Co-doped Cu-BTC (Cu-BTC, BTC = 1,3,5-benzene tricarboxylate) are among the MOFs employed in the conversion of FF [15–17]. However, most of the catalysts reported in the literature yield high amounts of by-products. Consequently, there is a need to design highly efficient catalytic systems for FF upgrading featuring high stability as well as enhanced activity and selectivity. In this study, the synthesis and characterization of **Cu-MOF** for the selective hydrogenation of FF to FA is presented.

2 Experimental

2.1 Materials and Chemicals

The chemicals; 4-aminobenzoic acid, isophthaloyl chloride and copper(II) nitrate trihydrate were purchased from Sigma-Aldrich and were all used as received. The organic

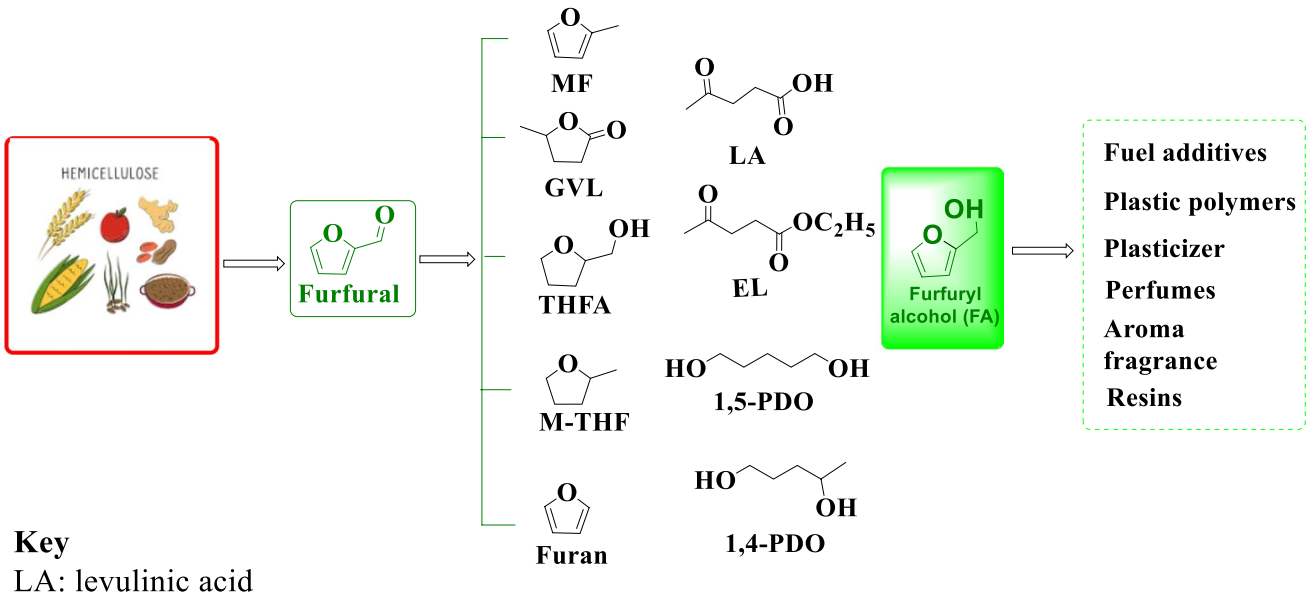

Key
LA: levulinic acid
EL: ethyl levulinate
THFA: tetrahydrofurfuryl alcohol
MF: 2-methylfuran
FA: furfuryl alcohol
1,5-PDO: 1,5-pentanediol
1,2-PDO: 1,2-pentanediol
MTHF: 2-methyltetrahydrofuran

Fig. 1 Catalytic upgrading of biomass-based FF into various value-added products [10]

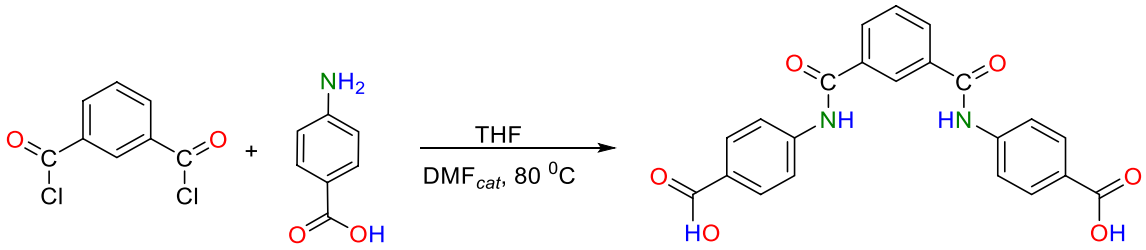

Scheme 1 Synthesis of **L1**

solvents; furfuryl alcohol (FA), tetrahydrofuran (THF), toluene, dimethylformamide (DMF), furfural (FF) and methanol (MeOH) were purchased from Sigma-Aldrich and were all utilized as received.

2.2 Synthesis and Characterisation of Ligand L1

(0.21 g, 1.55 mmol) 4-aminobenzoic acid was dissolved in THF (20 mL) and a few drops of DMF were added. Isophthaloyl dichloride (0.15 g, 0.74 mmol) was then added to the solution, and the resultant mixture was refluxed for 24 h. The hot solution was filtered, washed with hot THF (15 mL) and water (15 mL), and then dried overnight, resulting in a yellow solid product. Yield: 0.13 g (84%). Mp: decomposes without melting, onset occurs at 292 ℃. ^{1}H NMR (400 MHz, DMSO-d_6): (δ, ppm) 7.71 (t, CH, 1H, $^{3}J_{H-H} = 5$ Hz), 7.74–7.96 (m, 8H, CH), 8.18 (d, CH, 2H, $^{3}J_{H-H} = 1.6$), 8.58 (s, CH, 2H) and 10.73 (s, 2H, CH, NH)$_{amide}$. ^{13}C{^{1}H} NMR (100 MHz, DMSO-d_6): (δ, ppm) 120.05, 126.21, 127.68, 129.21, 130.72, 131.54, 135.32, 143.61, 165.85 and 167.39. Selected FT-IR peaks (ν_{max}: cm^{-1}): 3276 (NH)$_{amide,}$ 1683 (C=O)$_{acid}$ and 1609 (C=O)$_{amide}$. Elemental Analysis: (%): Calculated for $C_{22}H_{16}N_2O_6$: C, 65.35; H, 3.99; N, 6.93, Found: C, 65.37; H, 4.00; N, 6.96. HR-ESI-MS: Expected, $m/z = 404.10$, Found (negative): $m/z = 403.0918$ for [M-H]$^-$.

2.3 Synthesis of Cu-MOF $[Cu_2(L1)_2)\cdot 5DMF\cdot 4H_2O]_n$

$Cu(NO_3)_2\cdot 3H_2O$ (0.02 g, 0.10 mmol) and 4,4′-(isophthaloylbis(azanediyl))dibenzoic acid (0.02 g, 0.05 mmol) were

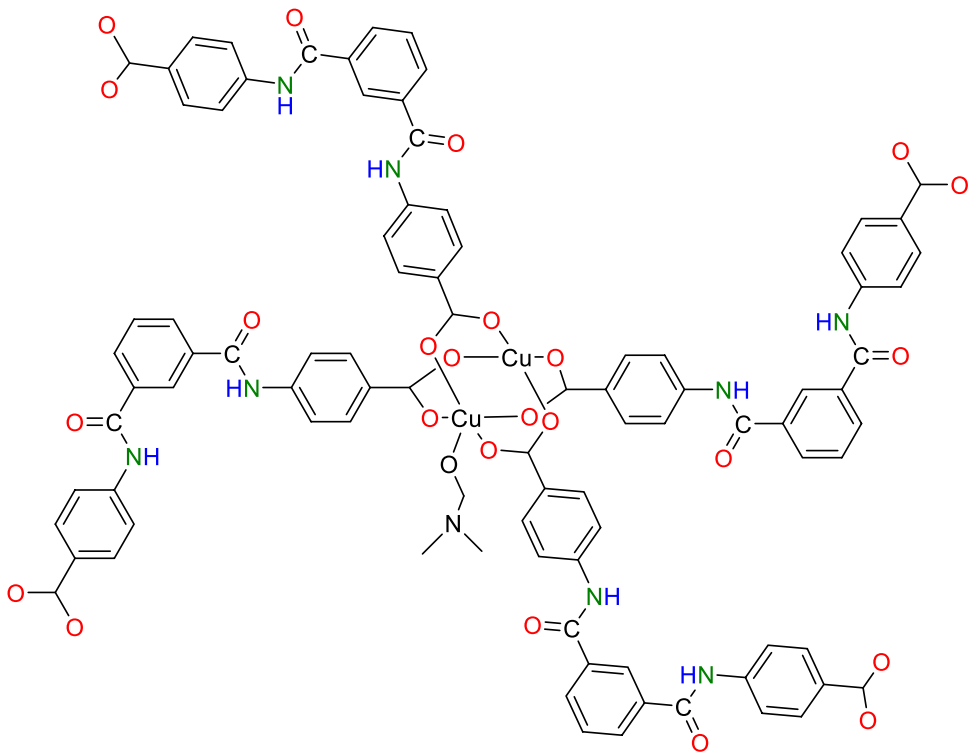

Fig. 2 Proposed structure of **Cu-MOF** depicting the coordination geometry around two Cu atoms

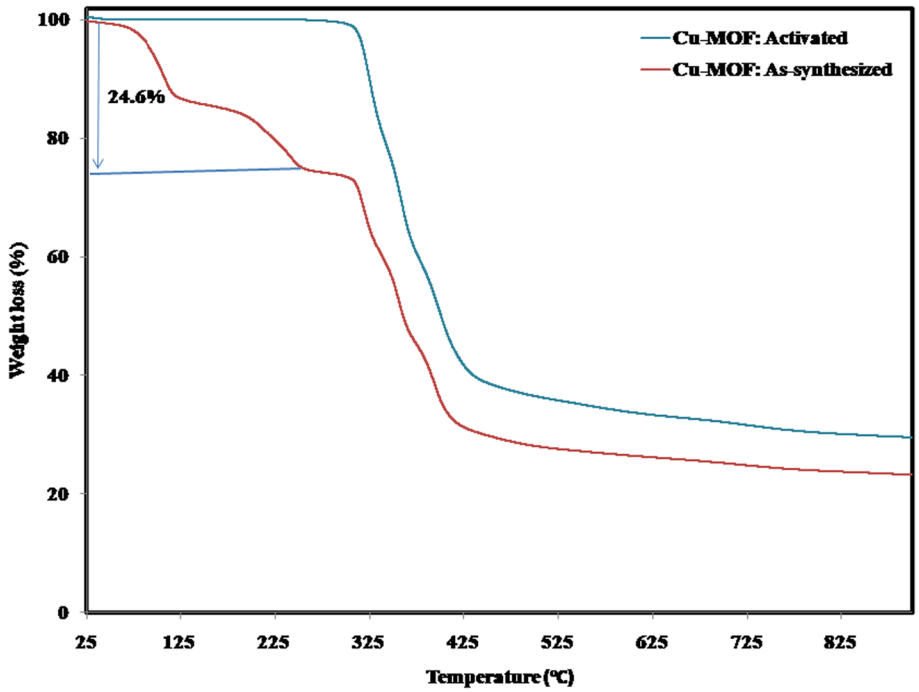

Fig. 3 TGA curves of activated and as-synthesized **Cu-MOF**

dissolved in DMF (5 mL). Blue clusters were obtained after slow evaporation of the solution at room temperature for 14 days. Yield: (70%). Selected FT-IR peaks (ν_{max}: cm^{-1}): 3274 $(NH)_{amide}$ and 1603 $(C{=}O)_{acid}$. Copper analysis: Found: 10.7% *m*/*m*. Elemental Analysis (%): Calculated for $Cu_2C_{59}H_{71}N_9O_{21}$ (1367.34): C, 51.75; H, 5.23; N, 9.28, Found: C, 51.26; H, 4.72; N, 8.98.

3 Characterization Techniques

Nuclear magnetic resonance spectra were recorded on a Bruker Ultrashield-500 MHz spectrometer (^1H: 500 MHz and $^{13}C\{^1H\}$: 100 MHz) in chloroform or dimethylsulfoxide solutions using tetramethylsilane as an internal standard ($\delta = 0$ ppm). X-ray photoelectron spectroscopy analysis was obtained with a Kratos Axis supra spectrometer using an Al K(alpha) source (15 mA, 0.15 eV). Survey scan and high resolution were carried out with an analysis area of 300×700 microns and pass energy of 160 eV. The chemical states were identified by using Casa XPS software version 2.3.22. The functional groups of the ligand and **Cu-MOF** were confirmed using Fourier-transform infrared spectroscopy which was recorded using IR-Affinity-1S FT-IR Spectrophotometer instrument fitted with an ATR probe. Powder diffraction patterns were measured on a Bruker D8 Advance X-ray diffractometer operating in a DaVinci geometry equipped with a Lynxeye detector using Cu Kα-radiation ($\lambda = 1.5406$ Å) at 298 K. X-rays were generated by an accelerating voltage of 30 kV and a current of 40 mA. A receiving slit of 0.6 mm and a primary and secondary slit of 2.5 mm were used. Samples were placed on a zero-background sample holder and scanned over a range of 4° to 40° in 2θ with a step size of 0.01° per second. Thermogravimetry analysis experiments were carried out on a TA Discovery Instrument TA-Q50 with a heating rate of 10 °C min^{-1} within a temperature range of 25–1000 °C under a dry nitrogen purge gas flow of 50 $mLmin^{-1}$. The samples were analyzed using the Tescan Vega scanning electron microscopy. The morphological studies were done using a Jeol-Jem 2100F electron transmission electron microscopy operating at a voltage of 200 kV. Melting points were determined using a Bůchi melting point apparatus B-540. Mass spectrometry was carried out on a Water Synapt G2 electrospray ionization mass spectrometer in the negative or positive-ion mode. Elemental analysis was recorded using a Thermo Scientific Flash 2000 Series CHNS-O Analyzer. Inductively coupled plasma optical emission spectroscopy analysis was performed on a SpectroArcros instrument calibrated using standards.

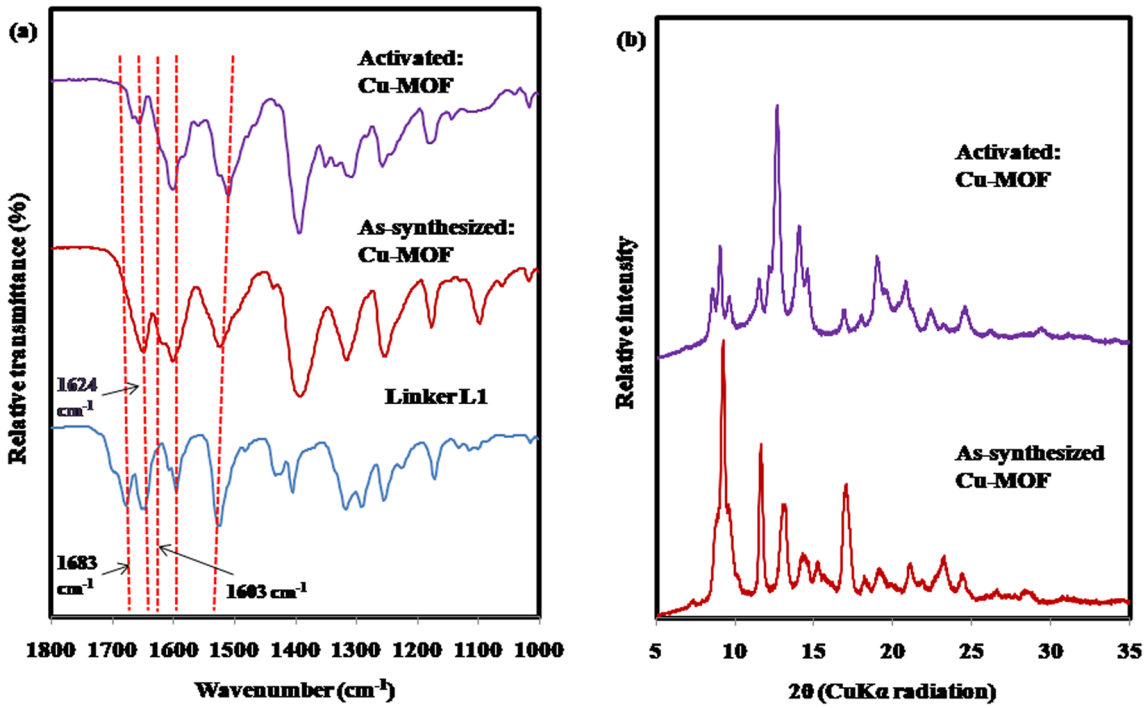

Fig. 4 **a** FT-IR spectra of **L1**, activated **Cu-MOF** and as-synthesized **Cu-MOF**, and **b** PXRD patterns of activated **Cu-MOF** and experimental **Cu-MOF**

4 Results and Discussion

4.1 Synthesis and Characterization of Ligand L1

Ligand **L1** was prepared following the modified reported procedure by Iftikhar [18]. 4,4′-(isophthaloylbis(azanediyl)) dibenzoic acid was fabricated by reacting 4-amino benzoic acid with the corresponding isophthaloyl dichloride in tetrahydrofuran for 24 h (Scheme 1). **L1** was characterized using high-resolution electrospray ionization mass spectrometry (HR-ESI-MS), elemental analysis (CHN), Fourier transform-infrared spectroscopy (FT-IR) and nuclear magnetic resonance (NMR) spectroscopy.

The successful synthesis of the ligand was corroborated by the presence of a singlet peak at 10.73 ppm in the ^{1}H NMR spectra of **L1**, which corresponds to the amide functionality (Figure SI 1). In addition, the rest of the aromatic resonances were observed from 7.71 ppm to 8.58 ppm. The $^{13}C\{^{1}H\}$ NMR spectrum for carboxamide ligand revealed aromatic carbon signals ranging from 120.05 ppm to 167.39 ppm. The amide carbon was the most deshielded signal observed at 167.39 ppm (Figure SI 2). All the peaks in the $^{13}C\{^{1}H\}$ NMR spectrum were successfully assigned with the help of a 2-dimensional HSQC spectrum. The HR-ESI-MS spectrum further provided additional evidence for the formation of the ligand by displaying the molecular ion peak at $m/z = 403.0918$ for $[M\text{-}H]^-$ ion (Figure SI 3).

The purity of the isolated ligand ($C_{22}H_{16}N_2O_6$) was confirmed by elemental analysis of **L1** (Calculated: C, 65.35; H, 3.99; N, 6.93, Found: C, 65.37; H, 4.00; N, 6.96). The FT-IR spectra of ligand **L1** revealed a broad absorption band at 3276 cm^{-1}, which was attributed to the NH stretching frequency. Additional strong FT-IR absorptions appeared at 1609 cm^{-1} and 1683 cm^{-1} assigned to $(C{=}O)_{amide}$ and $(C{=}O)_{acid}$, which are shown in Figure SI 4. The FT-IR absorption bands were similar to the literature values [18–20].

4.2 Synthesis and Characterizations of Cu-MOF

Cu-MOF was synthesized by dissolving 0.02 g of compound **L1** in 5 mL of DMF and adding 0.02 g of $Cu(NO_3)_2{\cdot}3H_2O$. After 14 days, blue clusters were obtained by slow evaporation at room temperature [21]. The framework is insoluble in organic solvents, such as ethanol, dimethylformamide, dimethyl sulfoxide, and methanol. **Cu-MOF** was

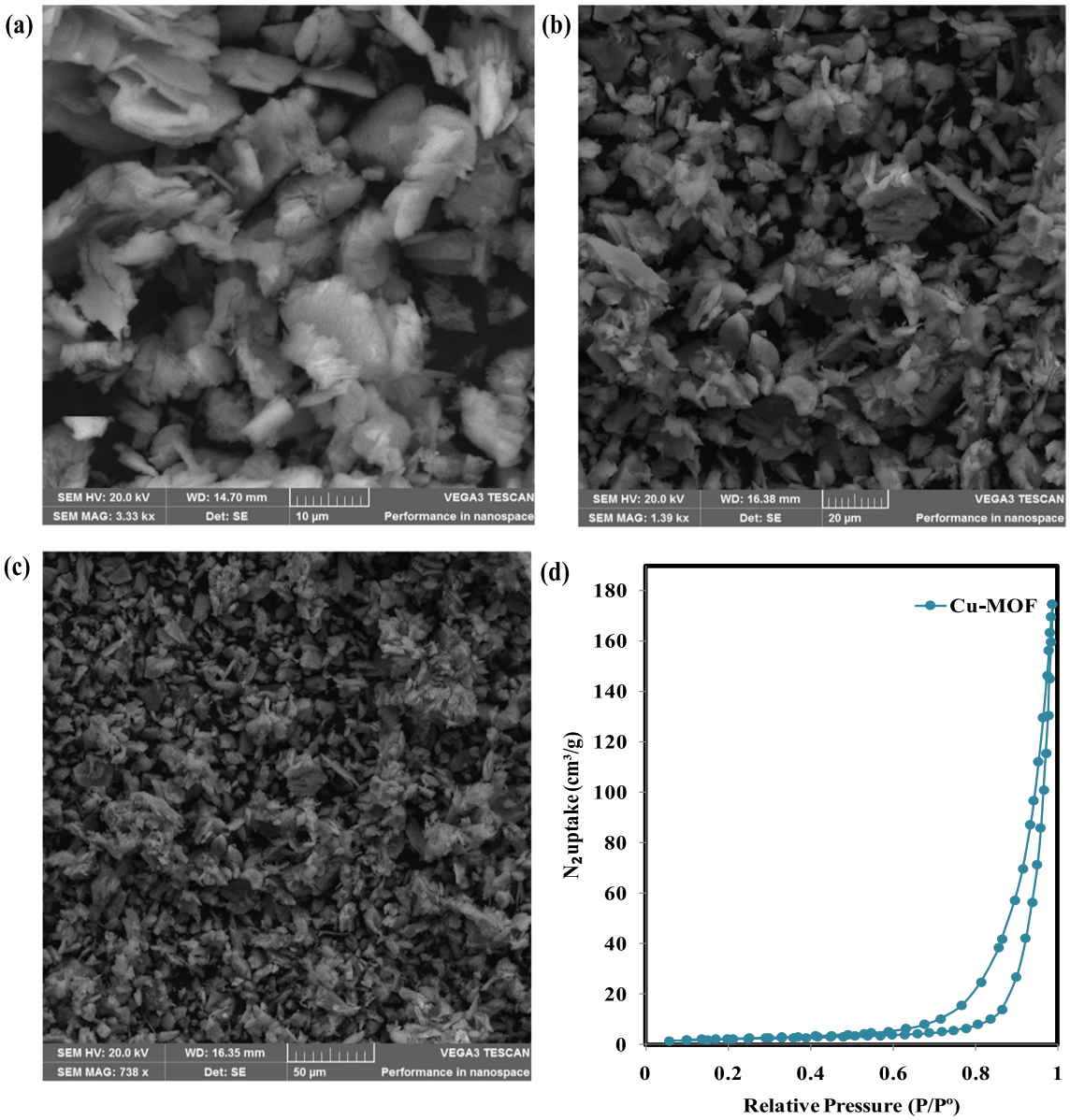

Fig. 5 SEM micrographs for **Cu-MOF** in different magnifications at **a** 10 µm, **b** 20 µm, **c** 50 µm and **d** N_2 sorption studies of **Cu-MOF**

synthesized and characterization results suggested the successful formation of the framework (Fig. 2) almost similar to copper(II) metal–organic framework reported in literature [22] by Malaza and co-workers. The **Cu-MOF** crystallized in monoclinic crystal system and $P2_1/c$ space group, where two Cu(II), two linkers, five DMF molecules and four water molecules constitute the asymmetric unit [22]. Each Cu(II) centre was coordinated to four oxygen atoms from the linkers and guest molecules to generate a copper paddlewheel SBU [$Cu_2C_4O_8$].

The thermal behaviour was investigated at temperatures ranging from 25 to 1000 °C and heated up at a rate of 10 °C/min under N_2 atmosphere and air-flow (Fig. 3). The TGA profile of **Cu-MOF** displayed a major weight loss of 24.6% in the region from 90 to 260 ℃, which was correlated to the

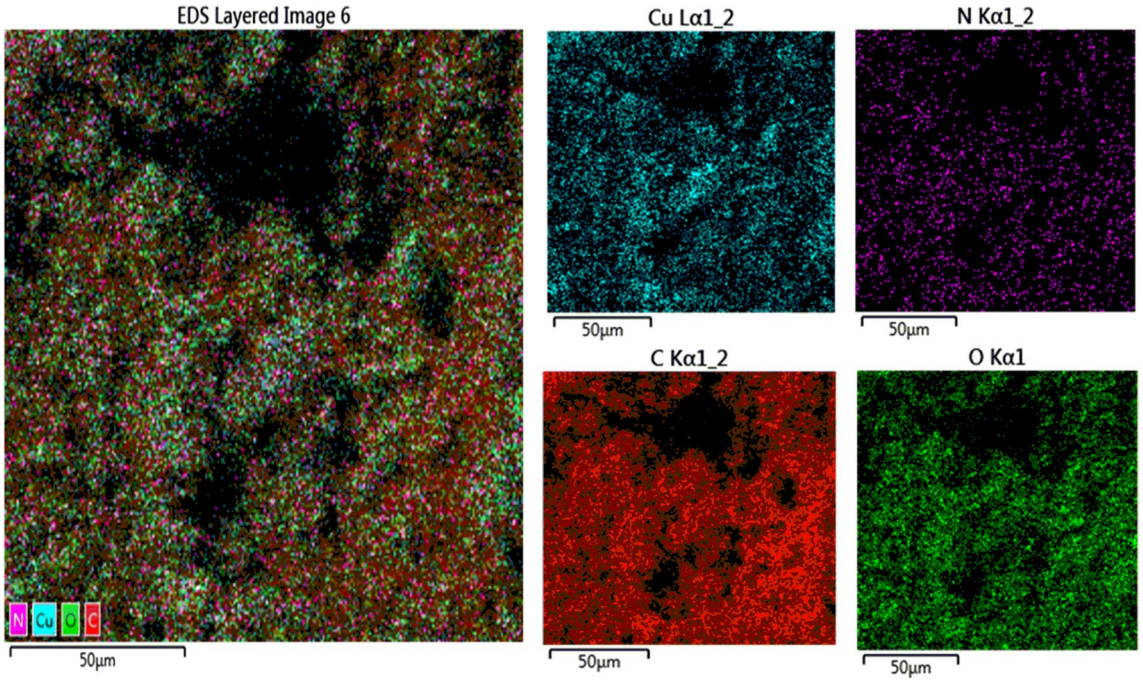

Fig. 6 Elemental mapping image for **Cu-MOF**

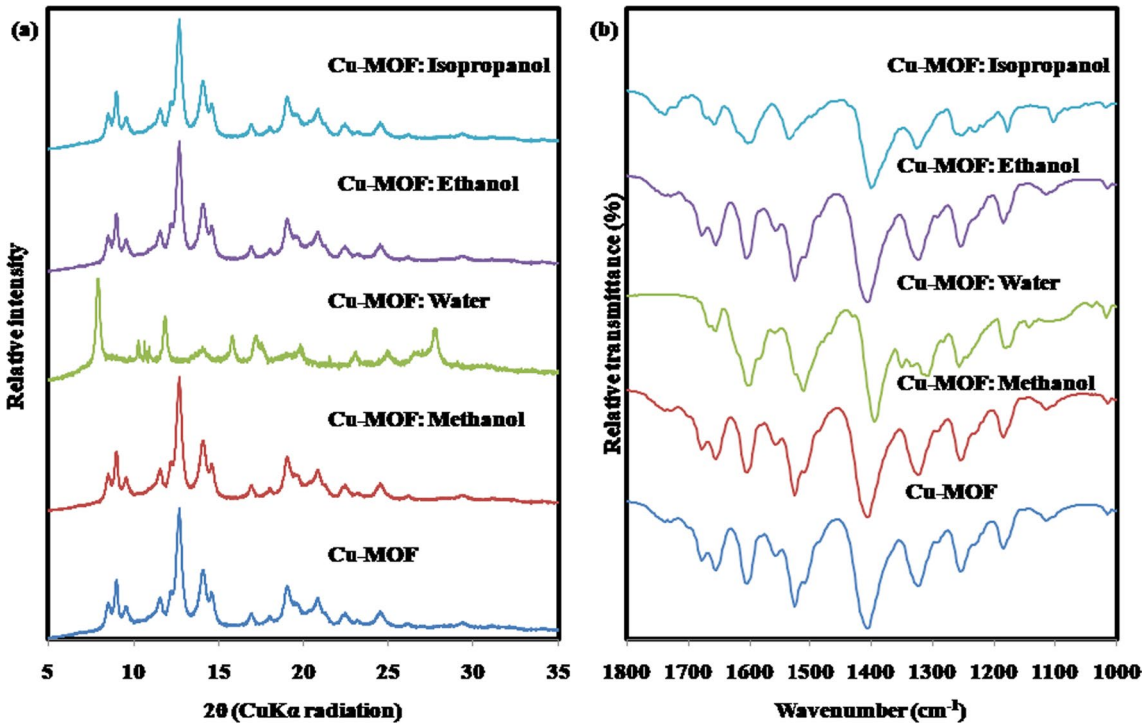

Fig. 7 **a** PXRD patterns of **Cu-MOF** soaked in different solvents and **b** FT-IR spectra of **Cu-MOF** soaked in different solvents

expulsion of five DMF molecules and four water molecules (Proposed formula: $[Cu_2(L1)_2)\cdot 5DMF\cdot 4H_2O]_n$. This prediction was based on our CHN elemental analysis results, ^1H NMR results (Figure SI 5) and single crystal data for **Cu-MOF** by Malaza and co-workers [22]. The decomposition of the framework structure was observed at 310 ^oC showing

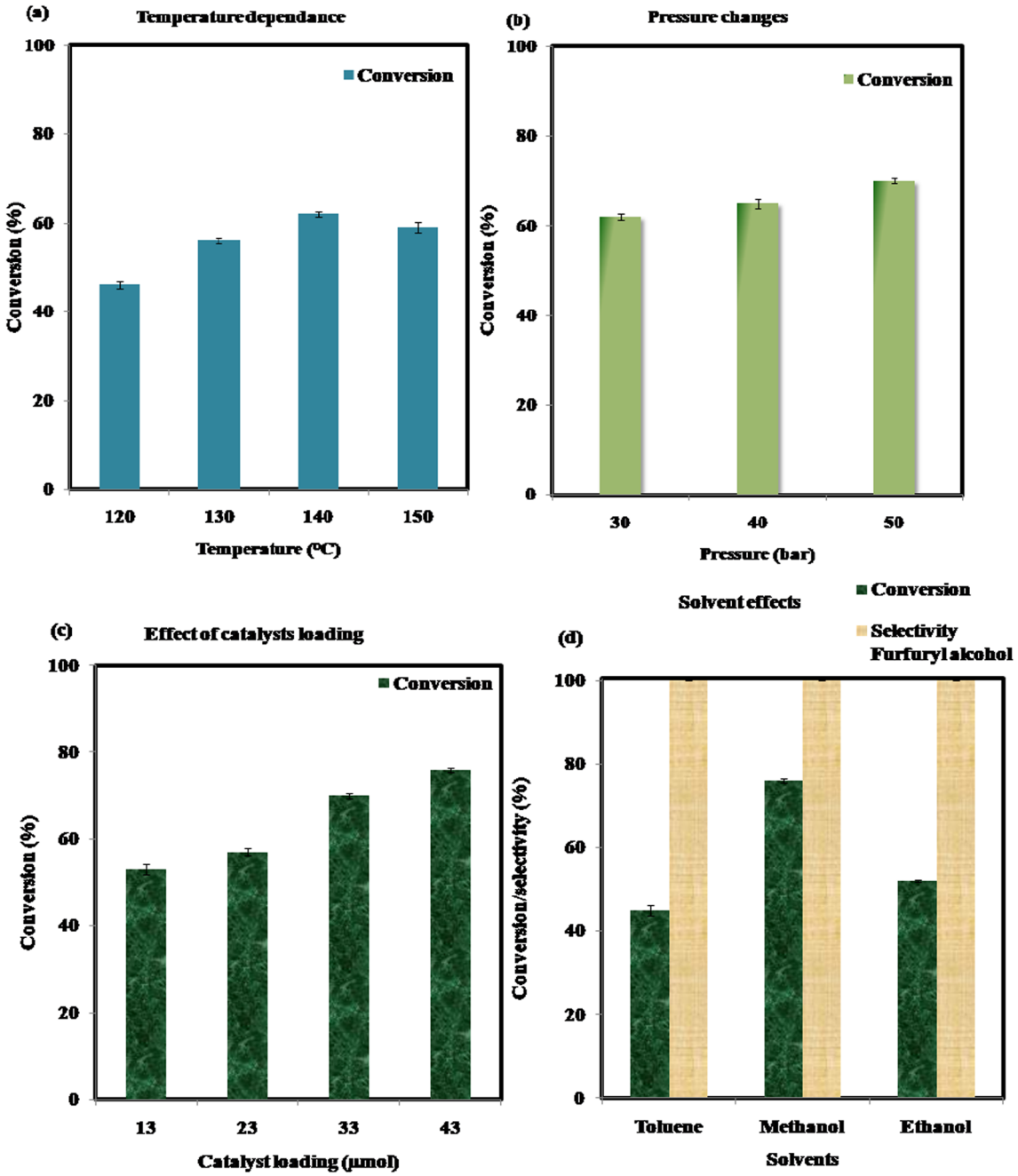

Fig. 8 **a** Effect of temperature. Conditions: Time (24 h), substrate (FF, 2.5 mmol), hydrogen gas (30 bar), methanol (5 mL) and **Cu-MOF** (33 µmol), **b** effect of pressure. Conditions: Temperature (140 °C), time (24 h), FF (2.5 mmol), methanol (5 mL) and **Cu-MOF** (33 µmol), **c** effect of catalyst loading. Conditions: Hydrogen gas (50 bar), time (24 h), methanol (5 mL), FF (2.5 mmol), pre-catalyst (**Cu-MOF**) and temperature (140 °C), **d** effect of solvent. Conditions: FF (2.5 mmol), Hydrogen gas (50 bar), solvent (5 mL), **Cu-MOF** (43 µmol), time (24 h) and temperature (140 °C). Conversion was determined by ^{1}H NMR spectroscopy

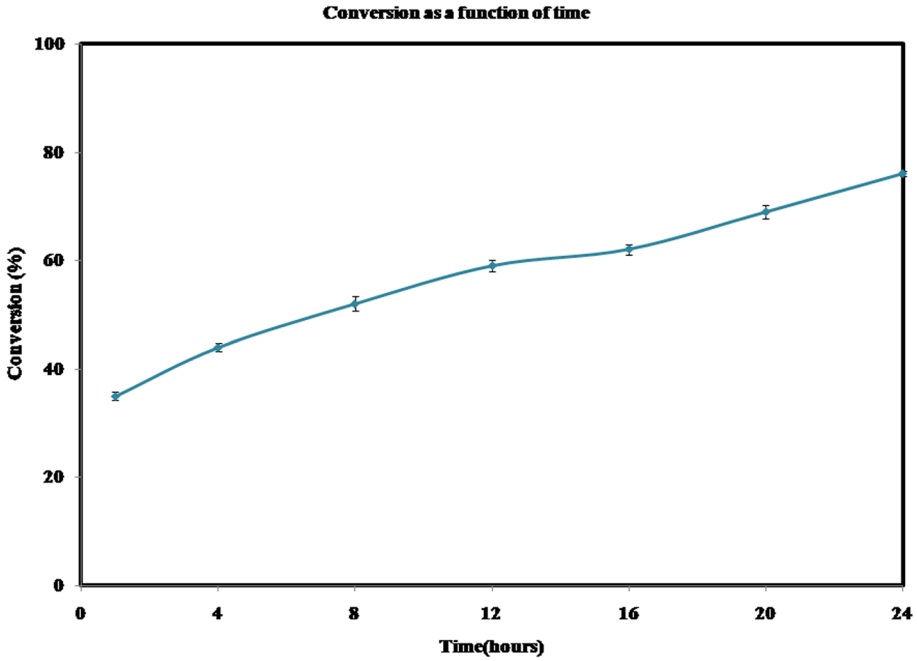

Fig. 9 Time-dependent study. Conditions: Hydrogen gas (50 bar), methanol (5 mL), FF (2.5 mmol), temperature (140 °C) and **Cu-MOF** (43 µmol)

remarkable thermal stability. A similar trend was observed in the TGA curve for TMA-Cu metal–organic framework [Trimesic acid (TMA)], reported by Sahiner and co-workers [23].

Cu-MOF was activated by soaking the framework in ethanol at room temperature for 36 h and then dried *in vacuo* at 100 °C for 24 h [24, 25]. TGA data that showed no weight loss until decomposition [25], proved that all of the guest molecules in activated **Cu-MOF** had been completely removed (Fig. 3). The FT-IR spectra of **L1**, as-synthesized **Cu-MOF** and activated **Cu-MOF** are illustrated in Fig. 4a. The carboxylate moiety stretching vibration (C=O) observed in the linker **L1** at 1683 cm^{-1} shifted to a lower absorption band at 1603 cm^{-1} in **Cu-MOF**. This observation confirmed the subsequent coordination of the Cu metal centre to the carboxylate moiety. The FT-IR spectrum for as-synthesized **Cu-MOF** showed carbonyl stretching vibration at 1624 cm^{-1} assigned to DMF molecules. Successful activation was confirmed by the disappearance of this band in activated **Cu-MOF**.

The phase purity of **Cu-MOF** was employed using PXRD analysis as depicted in Fig. 4b. The PXRD patterns of experimental **Cu-MOF** showed prominent diffraction peaks at 2θ values of 9.23, 11.67, 14.58, 15.37, 17.10, 19.41, 23.27 and 24.47 (Fig. 4b). Upon activation, a new phase transition was observed, as evidenced by the disappearance and appearance of new diffraction peaks. Remarkably, the structural framework remains intact after activation with insignificant loss of crystallinity [26].

ICP-OES analysis showed that **Cu-MOF** contains 10.7% *m/m* copper content. The detailed qualitative chemical analysis of **Cu-MOF** was conducted using SEM–EDX spectroscopy. SEM images of **Cu-MOF** showed a clusters like-structure (Fig. 5a–c), similar to the morphology reported by Omkaramurthy and co-workers [28]. EDX mapping of **Cu-MOF** revealed that Cu, N and O are homogenously distributed within the MOF matrix (Fig. 6), similar to the reported literature [27]. The presence of Cu, N and O elements in the framework was confirmed by the EDX spectrum (Figure SI 6).

The BET analysis of **Cu-MOF** was performed to elucidate the pore volume and specific area from N_2 adsorption–desorption isotherms (Fig. 5d). The pore volume and BET surface area of the framework were 0.27 cm^3/g, and 7.47 m^2/g, which was relatively lower than other MOFs reported in the literature [22, 30]. The N_2 sorption isotherms

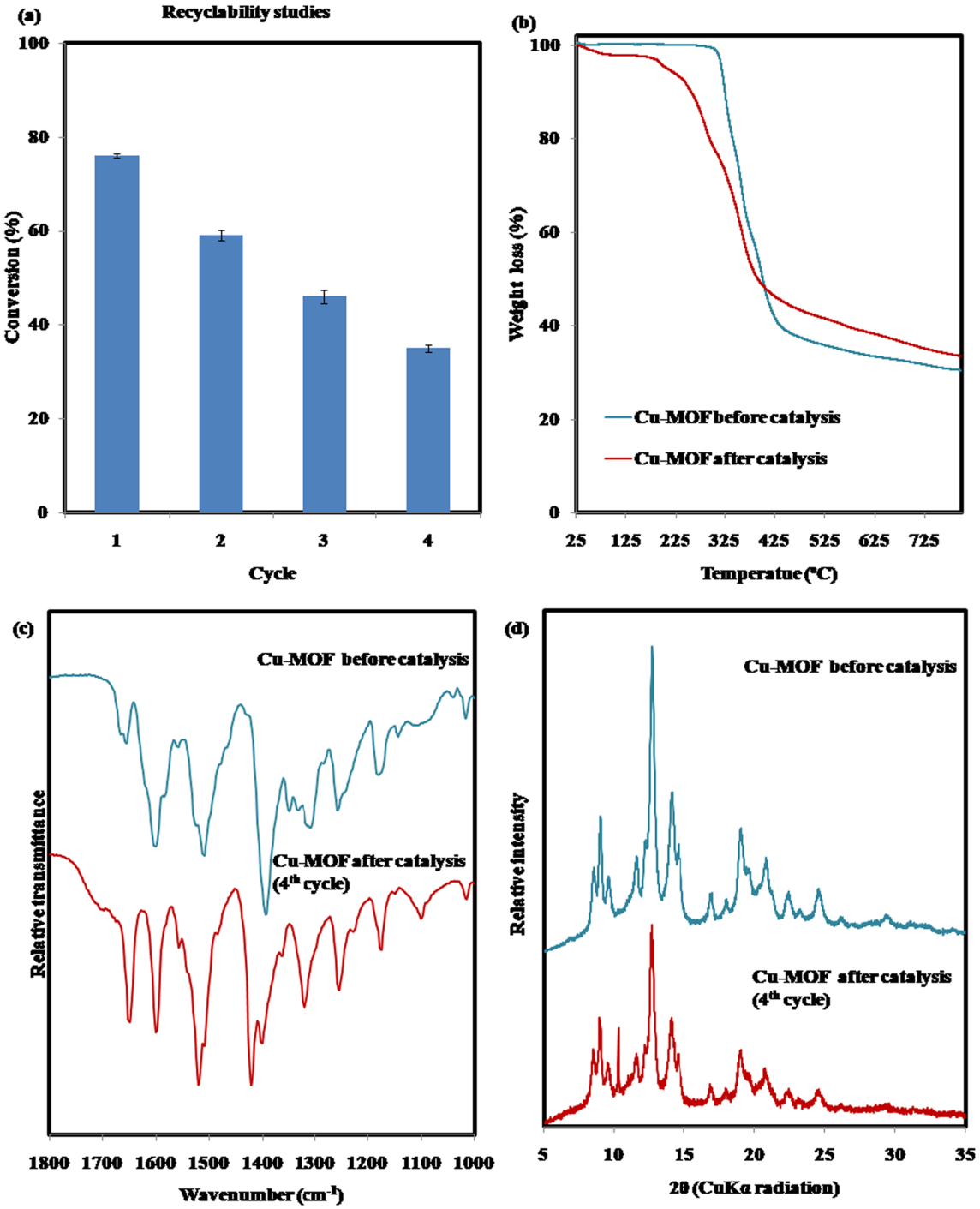

Fig. 10 **a** Recycling studies of **Cu-MOF** over four consecutive cycles, **b** TGA curves of **Cu-MOF** before and after catalysis (4th cycle), **c** FT-IR spectra of **Cu-MOF** before catalysis and after catalysis (4th cycle) and **d** PXRD patterns of **Cu-MOF** before catalysis and after catalysis (4th cycle)

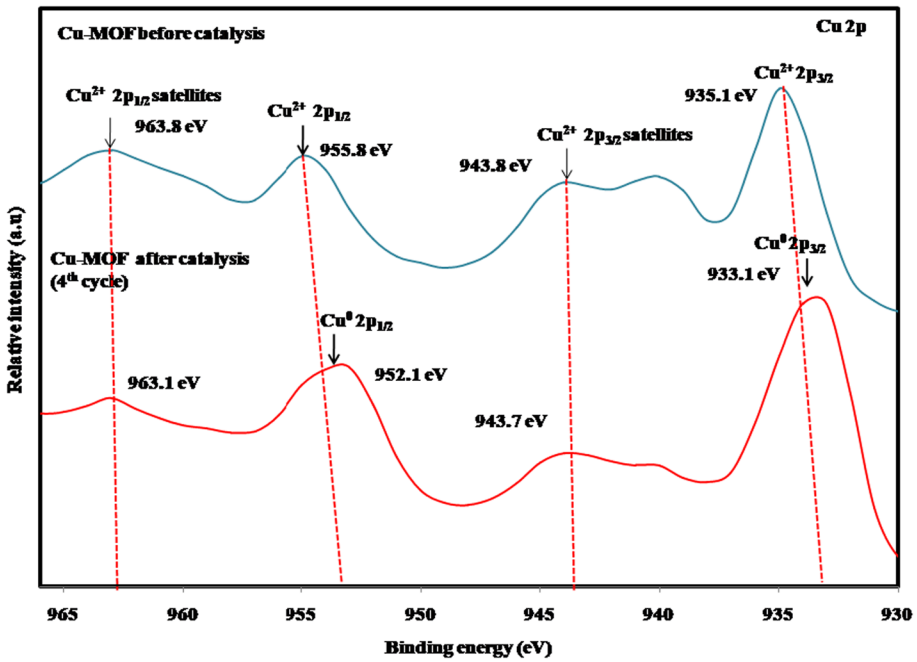

Fig. 11 XPS analysis of **Cu-MOF** before and after catalysis (4th cycle) showing Cu 2p core-level spectra

revealed a typical type I isotherm, assigned to microporous materials [31, 32].

5 Chemical Stability Tests

Activated **Cu-MOF** was immersed in different solvents for 24 h to determine their chemical stability under different operating environments [33–35]. The PXRD analysis results demonstrated that there was no structural alteration to the framework. Notably, the diffraction pattern of **Cu-MOF** in the presence of alcohols revealed that the structure was preserved. Howbeit, **Cu-MOF** in water showed a crystalline to crystalline transformation (Fig. 7a).

According to the FT-IR analysis of **Cu-MOF** soaked in solvents, the carboxylate moiety frequency found at 1603 cm^{-1} was not altered under various chemical environments (Fig. 7b). This study indicated that the carboxylate binding mode coordinated to the Cu^{2+} site was preserved under different chemical conditions. In addition, the C=O and NH stretching vibration peaks was present in all spectra.

5.1 Catalytic Hydrogenation of FF Using Cu-MOF

The activated **Cu-MOF** was evaluated for the hydrogenation of FF to FA. The influence of temperature, catalyst amount, solvent, reaction time and hydrogen pressure on the selectivity and conversion was explored to obtain the optimal conditions. In all instances, FA was produced as the only product with no side products detected (Figure SI 7). Initially, temperature variation studies were investigated in a range from 120 °C to 150 °C as depicted in Fig. 8a. As a result of the improved rate of catalysis, the conversion of FF increased significantly from 46 to 62% when the hydrogenation reaction temperature rose from 120 to 140 °C. Based on this observation, 140 °C was selected as the optimal reaction temperature. Similarly to other frameworks, 140 °C gave an impressive conversion of FF > 60% [36, 37]. Surprisingly,

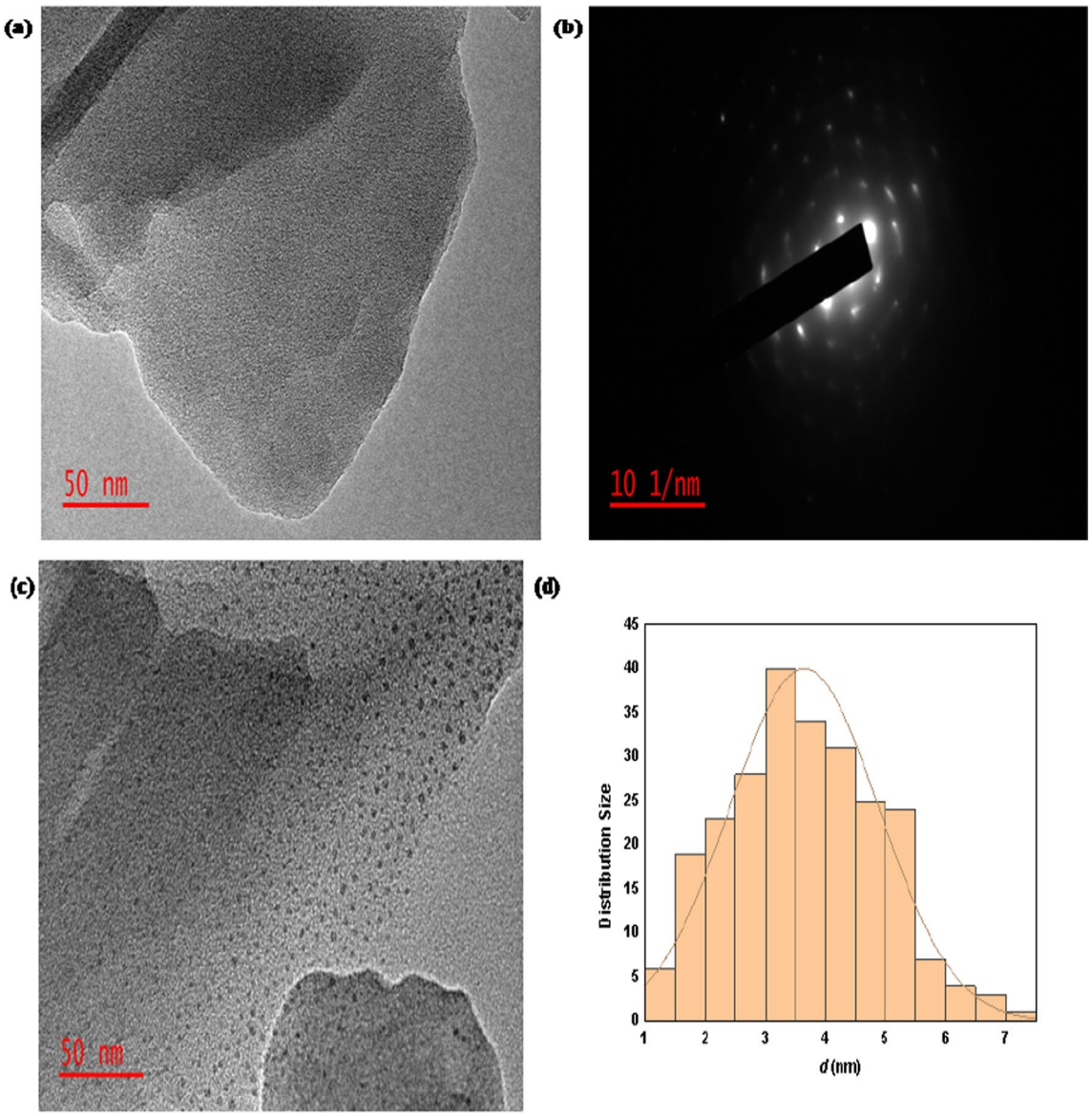

Fig. 12 **a** HR-TEM image for **Cu-MOF** before catalysis at 50 nm scale, **b** insert showing SAED pattern for **Cu-MOF**, **c** HR-TEM image for **Cu-MOF** after catalysis (4th cycle) at 50 nm scale and **d** Histogram of the particle size distribution for **Cu-MOF** after catalysis (4th cycle)

when the temperature was raised to 150 °C, the conversion decreased signifying possible catalyst deactivation.

The effect of pressure was investigated in 30 to 50 bar pressure range at 140 ℃ (Fig. 8b). The conversion of FF was increased from 62 to 65% with increased hydrogen pressure from 30 to 40 bar, while maintaining selectivity to FA (100%). At 50 bar, the conversion of FF attained was 70%, selected as the best pressure for further investigations. Koley and co-workers hypothesized that an increase in the concentration of H_2 in the reaction mixture was responsible for the higher conversion of FF over the $Cu/CuFe_2O_4$@C-A catalyst [16].

The influence of catalyst loading on the catalytic performance was studied. The load was varied from 13 µmol to 43 µmol (Fig. 8c). It was observed that the conversion of FF decreased from 57 to 53% as the amount of catalyst decreased from 23 to 13 µmol. The pre-catalyst had insufficient active sites at a lower catalyst amount [38]. As the catalyst loading increased from 33 to 43 µmol, the conversion of FF was enhanced. Thus, 43 µmol was selected as the optimal catalyst loading.

The effect of solvent systems was studied using **Cu-MOF**. Ethanol, toluene and methanol were utilized as the solvents in FF upgrading (Fig. 8d). Compared to ethanol,

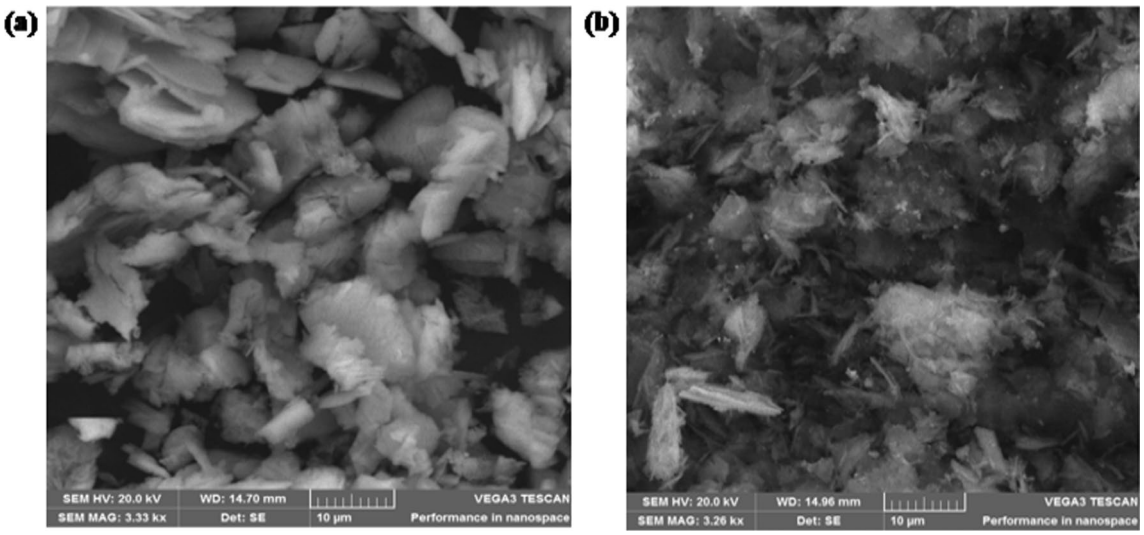

Fig. 13 SEM images of **a Cu-MOF** before catalysis and **b Cu-MOF** after catalysis (4th cycle)

methanol gave the highest conversion of FF (76%). Switching from methanol as the solvent to toluene gave the least conversion of FF (45%), a similar trend has been observed in the literature [39–41]. The influence of time was also conducted from 1 to 24 h, keeping all other parameters constant (Fig. 9). **Cu-MOF** exhibited low activity over the first 4 h, indicating an induction period is necessary to ensure diffusion of the H_2 into the solvent and Cu^{2+} metal active sites.

The highest turnover frequency (TOF) of up to 20 h^{-1} was obtained within 1 h. Clearly, the conversion of FF rapidly increased from 35 to 76% with a prolonged reaction time from 1 to 24 h and 24 h was chosen as the optimal time for further studies. This is longer than the reaction times described in the literature, which normally needed 1 to 8 h for enhanced selectivity [37, 42]. Interestingly, the hydrogenation performance for this study was highly chemoselective to FA.

Cu-MOF and the corresponding metal salt used to construct the framework were screened for hydrogenation of FF in MeOH under optimal conditions (50 bar, 140 °C, 24 h). $Cu(NO_3)_2{\cdot}3H_2O$ exhibited minor conversion (7%). **Cu-MOF** (Cu metal centre) showed impressive activity with a conversion of FF (76%) and selectivity to FA (100%) and was used for further investigations. Cu (active sites) are known for the activation of C=O bonds and dissociation of H_2. The strong interaction between the linker (Brønsted acid site) and Cu (Lewis acid site) plays a significant role in improved hydrogenation performance [37]. Cu-MOF outperformed other catalysts that had been previously reported because of its chemoselectivity, despite the low activity [15, 36, 43].

5.2 Recycling Studies

Recycling studies for **Cu-MOF** was conducted to determine the durability of the catalyst. After the hydrogenation reaction, the crude mixture was filtered and washed with methanol and dried *in vacuo* overnight. The recovered catalyst was re-evaluated under optimal reaction conditions [44]. The catalyst could be recycled up to four consecutive runs with a significant loss in catalytic activity (Fig. 10a). This observation might be due to the partial deactivation of the active species with each cycle. The spent catalyst was characterized using TGA, FT-IR, PXRD, SEM–EDX, HR-TEM and XPS spectroscopy.

TGA for recovered catalyst **Cu-MOF** showed that the thermal stability of the framework was altered in comparison to the parent MOF before catalysis as depicted in Fig. 10b [45]. The FT-IR spectrum for the spent catalyst was altered after recycling due to the partial catalyst decomposition (Fig. 10c), which is in agreement with the PXRD pattern results. Notably, the PXRD pattern for **Cu-MOF** showed changes in the structural integrity after the 4th cycle (Fig. 10d).

The XPS spectra showed the existence of Cu, N and O elements in **Cu-MOF** (Fig. 11). The deconvoluted Cu 2p core level XPS spectra for the parent framework revealed binding energies (BE) peaks at 935.1 eV and 955.8 eV, assigned to Cu $2p_{3/2}$ and Cu $2p_{1/2}$, respectively. **Cu-MOF s**pectra exhibited binding energies peaks of Cu $2p_{3/2}$ satellite and Cu $2p_{1/2}$ satellite at 943.8 eV and 963.8 eV associated with Cu^{2+} species. Similar observations were made by Ruoff and co-workers for copper

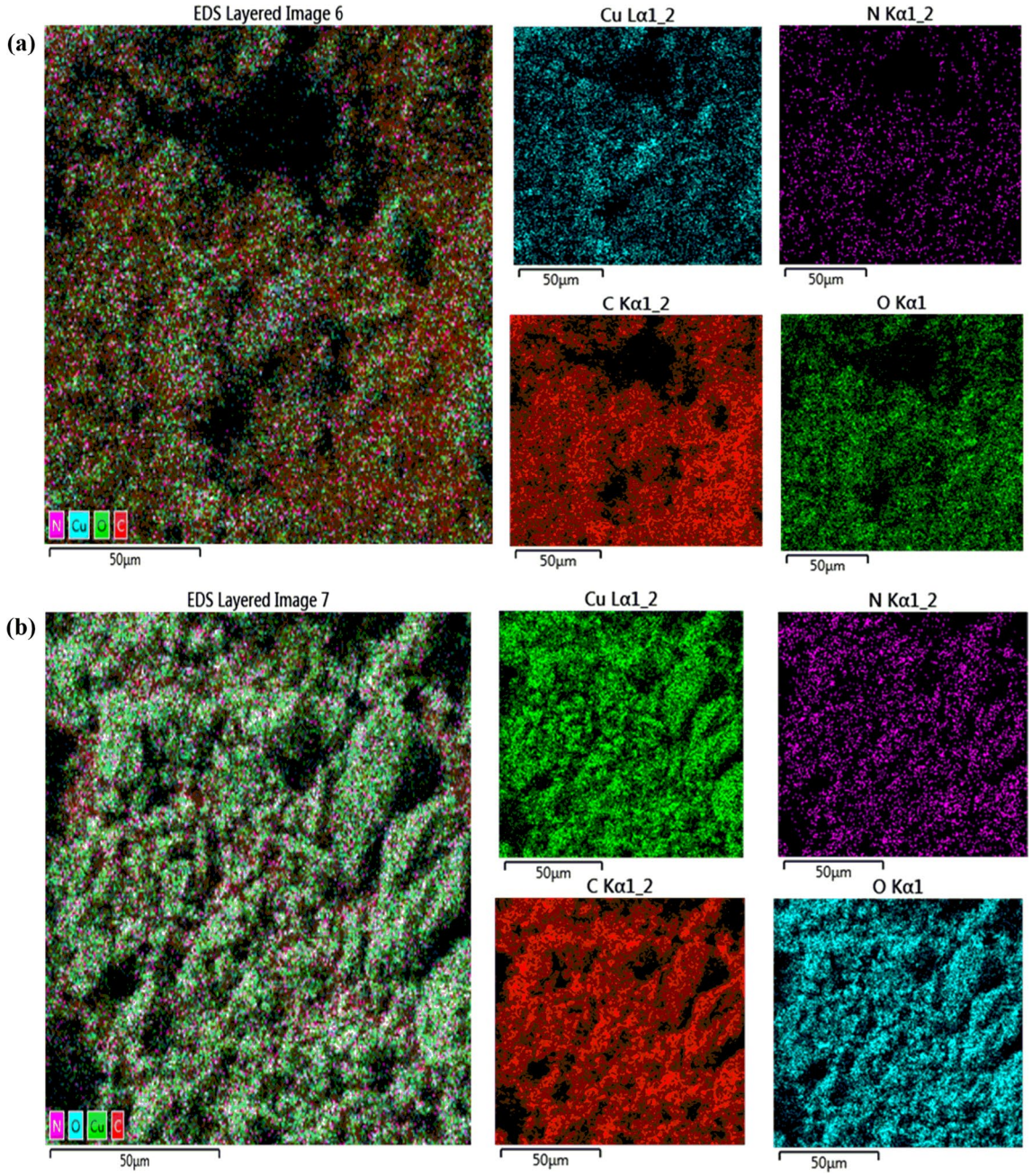

Fig. 14 EDX mapping images for **a Cu-MOF** before catalysis and **b Cu-MOF** after catalysis (4th cycle)

1,3,5-Triamino-2,4,6-benzenetriol metal–organic framework [46].

The electronic environment of Cu before and after catalysis was determined by XPS analysis. The binding energies of the Cu 2p core level spectra significantly changed, which signifies that both Cu^{2+} and Cu^{0} as active centres (Fig. 11). The Cu 2p XPS region for **Cu-MOF** after catalysis (4th cycle) showed the binding energies located at 933.1 eV and 952.1 eV assigned to Cu^{0} species [47, 48]. Moreover, the presence of weak satellite peaks also suggested the presence of Cu^{2+} species. According to the HR-TEM and XPS analysis results, a significant difference in oxidation state was observed.

HR-TEM images for **Cu-MOF** before catalysis exhibited a sheets-like structure (Fig. 12a and Figure SI 8), which is consistent with the previous report by Patil and co-workers [29]. Furthermore, the crystalline nature of **Cu-MOF**

was further confirmed by selected area electron diffraction (Fig. 12b), which is similar to the PXRD analysis results.

Particularly, HR-TEM images after catalysis were collected to check for the formation of Cu^0, as depicted in Fig. 12c. Homogeneously dispersed Cu^0 was observed on the spent **Cu-MOF** with a standard deviation of ± 1.3 nm and a uniform average particle size diameter of 3.5 nm (Fig. 12d).

SEM images revealed that the morphology of **Cu-MOF** was affected during catalysis (Fig. 13). A closer look at the EDX spectra of the framework before and after catalysis showed the presence of all constituent elements, similar to what has been reported in the literature reports [49]. Elemental mapping demonstrated that the Cu atoms were fairly distributed throughout the MOF matrix (Fig. 14).

6 Conclusion

A new **Cu-MOF** was facilely constructed by solvent evaporation method and was characterized using Brunauer-Emmet-Teller (BET), inductively coupled plasma-optical emission spectroscopy, high-resolution transmission electron microscopy, X-ray photoelectron spectroscopy, Fourier transform-infrared spectroscopy, powder X-ray diffraction and scanning electron microscopy-energy dispersive X-ray spectroscopy. XPS analysis confirmed the presence of Cu^{2+}, N and O in the structure of the **Cu-MOF** and is in good agreement with the proposed structure of the catalyst. At optimized operating conditions, **Cu-MOF** showed conversion of FF (76%) and selectivity towards FA (100%). The framework was reused four times with a substantial loss of catalytic activity. There was significant drop in catalytic activity, based on TGA, FT-IR, PXRD, SEM–EDX, HR-TEM and XPS spectroscopy results. One way of improving the catalytic activity involves tailoring the organic linker in the MOF. Varying the metal centres in the MOF (active sites) might be another approach to enhance activity under mild conditions. Another strategy is to fabricate core–shell-structured MOF-based composites by coating the MOF with other functional materials (e.g., zeolites or enzymes). These approaches offer the possibility to fine-tune the framework catalytic stability.

Supplementary Information The online version contains supplementary material available at https://doi.org/10.1007/s10904-024-03163-8.

Acknowledgements We gratefully acknowledge the University of Johannesburg, Research Centre for Synthesis and Catalysis, and Spectrum department for making their facilities available. Our profound gratitude also goes to Mr Mutshinyalo Nwamadi and Mrs Orienda Molahlegi for their assistance with the nuclear magnetic resonance spectroscopy and powder X-ray diffraction, respectively.

Author Contributions Conceptualization, B.C.E.M and L.C.M.; methodology, B.C.E.M and L.C.M.; validation, P.S.M., B.C.E.M, G.M and L.C.M.; formal analysis and investigation P.S.M.; resources, B.C.E.M and L.C.M; data curation, P.S.M.; analysis, P.S.M.; software: P.S.M; writing—original draft preparation, P.S.M.; writing—review and editing B.C.E.M., L.C.M, G.M and P.S.M.; visualization, P.S.M., G.M, B.C.E.M, L.C.M. and G.M.; supervision, B.C.E.M, G.M and L.C.M.; Project administration, B.C.E.M.; funding acquisition, B.C.E.M and L.C.M. All authors have read and agreed to the published version of the manuscript.

Funding Open access funding provided by University of Johannesburg. The Royal Society-Future Leaders-African Independent Researcher Fellowship supported by Global Challenges Research Fund (Fellowship ref: 191779) and the National Research Foundation of South Africa (Grant Numbers: SRUG22052514577) funded this research.

Data Availability The datasets that support the findings of this study are available in the supplementary material of this article.

Declarations

Conflict of Interests There are no conflicts of interest to declare.

References

1. R.F. Perez, M.A. Fraga, Hemicellulose-derived chemicals: one-step production of furfuryl alcohol from xylose. Green Chem. **16**, 3942 (2014). https://doi.org/10.1039/C4GC00398E
2. M.J. Climent, A. Corma, S. Iborra, Conversion of biomass platform molecules into fuel additives and liquid hydrocarbon fuels. Green Chem. **16**, 516 (2014). https://doi.org/10.1039/C3GC41492B
3. K. Sivabalan, S. Hassan, H. Ya, J. Pasupuleti, A review on the characteristic of biomass and classification of bioenergy through direct combustion and gasification as an alternative power supply. J. Phys. Conf. Ser. **1831**, 012033 (2021). https://doi.org/10.1088/1742-6596/1831/1/012033
4. R.F. Perez, S.J. Canhaci, L.E. Borges, M.A. Fraga, One-step conversion of xylose to furfuryl alcohol on sulfated zirconia-supported Pt catalyst-balance between acid and metal sites. Catal. Today **289**, 273 (2017). https://doi.org/10.1016/j.cattod.2016.09.003
5. H. Li, Z. Fang, R.L. Smith, S. Yang, Efficient valorization of biomass to biofuels with bifunctional solid catalytic materials. Prog. Energ. Combu Sci. **55**, 98 (2016). https://doi.org/10.1016/j.pecs.2016.04.004
6. H.J. Brownlee, C.S. Miner, Industrial development of furfural. Ind. Eng. Chem. **40**, 201 (1948). https://doi.org/10.1021/ie50458a005

7. C.H. Christensen, J. Rass-Hansen, C.C. Marsden, E. Taarning, The renewable chemicals industry. Chemsuschem **1**, 283 (2008). https://doi.org/10.1002/cssc.200700168
8. W. De Jong, G. Marcotullio, Overview of biorefineries based on co-production of furfural, existing concepts and novel developments. Int. J. Chem. React. Eng. **8**, 1 (2010). https://doi.org/10.2202/1542-6580.2174
9. T.L. Yong, N. Mohamad, N.N.M. Yusof, Furfural production from oil palm biomass using a biomass-derived supercritical ethanol solvent and formic acid catalyst. Proc. Eng. **148**, 392 (2016). https://doi.org/10.1016/j.proeng.2016.06.495
10. J. Long, Y. Xu, W. Zhao, H. Li, S. Yang, Heterogeneous catalytic upgrading of biofuranic aldehydes to alcohols. Front. Chem. **7**, 529 (2019). https://doi.org/10.3389/fchem.2019.00529
11. R.V. Sharma, U. Das, R. Sammynaiken, A.K. Dalai, Liquid phase chemo-selective catalytic hydrogenation of furfural to furfuryl alcohol. Appl Catal. A: Gen. **454**, 127 (2013). https://doi.org/10.1016/j.apcata.2012.12.010
12. X. Li, P. Jia, T. Wang, Furfural: a promising platform compound for sustainable production of C4 and C5 chemicals. ACS Catal. **6**, 762 (2016). https://doi.org/10.1021/acscatal.6b01838
13. L. Liu, H. Lou, M. Chen, Selective hydrogenation of furfural over Pt-based and Pd-based bimetallic catalysts supported on modified multiwalled carbon nanotubes (MWNT). Appl. Catal. A **550**, 1 (2018). https://doi.org/10.1016/j.apcata.2017.10.003
14. A. Herbst, C. Janiak, MOF catalysts in biomass upgrading towards value-added fine chemicals. CrystEngComm **19**, 4092 (2017). https://doi.org/10.1039/C6CE01782G
15. K.W. Golub, T.P. Sulmonetti, L.A. Darunte, M.S. Shealy, C.W. Jones, Metal-organic framework derived Co/Cu-Carbon nanoparticle catalysts for furfural hydrogenation. ACS Appl. Nano Mater. **2**, 6040 (2019). https://doi.org/10.1021/acsanm.9b01555
16. P. Koley, S.C. Shit, B. Joseph, S. Pollastri, Y.M. Sabri, E.L.H. Mayes, L. Nakka, J. Tardio, J. Mondal, Leveraging Cu/CuFe2O4-catalyzed biomass-derived furfural hydrodeoxygenation: a nanoscale metal−organic framework template is the prime key. ACS Appl. Mater. Interfaces **12**, 21682 (2020). https://doi.org/10.1021/acsami.0c03683
17. Y. Wang, S. Sang, W. Zhu, L. Gao, G. Xiao, CuNi@C catalysts with high activity derived from metal-organic frameworks precursor for conversion of furfural to cyclopentanone. Chem. Eng. J. **299**, 104 (2016). https://doi.org/10.1016/j.cej.2016.04.068
18. K. Iftikhar, S. Murtaza, N. Kousar, A. Abbas, M.N. Tahir, Aminobenzoic acid derivatives as antioxidants and cholinesterase inhibitors: synthesis, biological evaluation and molecular docking studies. Acta Pol. Pharm-Drug. Res. **75**, 385 (2018)
19. O.V. Enearepuadoh, D.E. Dixon, Synthesis, characterization and adsorption study of metal-organic framework of copper(II) benzene-1,4-dicarboxylate (Cu-MOF) on crude oil. Mater. Chem. Phys. **2**, 1 (2021). https://doi.org/10.23977/pmcp.2021.020101
20. P.S. Moyo, G. Mehlana, L.C. Matsinha, B.C.E. Makhubela, Highly efficient hydrogenation of furfural to valuable products catalysed by Rh(III), Pd(II), Ni(II), Fe(II) and Ru(II) half-sandwich picolinamide and the SBA-15 supported molecular complexes as pre-catalysts. Appl. Organomet. Chem. (2023). https://doi.org/10.1002/aoc.7166
21. P. Howlader, P.S. Mukherjee, Solvent-directed synthesis of molecular cage and metal-organic framework of copper(II) paddlewheel cluster. Isr. J. Chem. **59**, 1 (2018). https://doi.org/10.1002/ijch.201800155
22. S.S.P. Malaza, G. Mehlana, O. Cheung, R. Hunter, B.C.E. Makhubela, Crystalline $Cu^{(II)}$ metal–organic frameworks based on a carboxamide pincer ligand and an $N^{CO}N^{CO}N$-$Pd^{(II)}$ pincer complex. CrystEngComm **23**, 7418 (2021). https://doi.org/10.1039/D1CE00999K
23. N. Sahiner, K. Sel, F.O. Ozturk, S. Demirci, G. Terzi, Facile synthesis and characterization of trimesic acid-Cu based metal-organic frameworks. Appl. Surf. Sci. **314**, 663 (2014). https://doi.org/10.1016/j.apsusc.2014.07.023
24. N. Makuve, B.C.E. Makhubela, J. Dhakwa, G. Mehlana, Hydrogenation of CO_2 to formate using a cadmium-based metal–organic framework impregnated with nanoparticles. Int. J. Sci. Dev. Res. **6**, 30 (2021). https://doi.org/10.3390/inorganics10030030
25. X. Liang, P. Wang, C. Li, M. Yuan, Q. Shi, J. Dong, The activation of Co-MOF-74 with open metal sites and their corresponding CO/N_2 adsorptive. Microporous Mesoporous Mat. **320**, 111109 (2021). https://doi.org/10.1016/j.micromeso.2021.111109
26. Y. Han, M. Zhang, Y. Zhang, Z. Zhang, Copper immobilized at a covalent organic framework: an efficient and recyclable heterogeneous catalyst for the Chan-Lam coupling reaction of aryl boronic acids and amines. Green Chem. **20**, 4891 (2018). https://doi.org/10.1039/C8GC02611D
27. P.S. Moyo, B. Vatsha, G. Mehlana, L.C. Matsinha, B.C.E. Makhubela, Selective Cu and Ni-MOFs as pre-catalysts for the hydrogenation of furfural to furfuryl alcohol. Dalt. Trans. (2023). https://doi.org/10.1039/D3DT00671A
28. B.M. Omkaramurthy, G. Krishnamurthy, S. Foro, Synthesis and characterization of mesoporous crystalline copper metal–organic frameworks for electrochemical energy storage application. SN Appl. Sci. **2**, 1 (2020). https://doi.org/10.1007/s42452-020-2051-6
29. S.A. Patil, N.K. Shrestha, A.I. Inamdar, C. Bathula, J. Jung, S. Hussain, G. Nazir, M. Kaseem, H. Im, H. Kim, Bimetallic Cu/Fe MOF-based nanosheet film *via* binder-free drop-casting route: a highly efficient urea-electrolysis catalyst. Nanomaterials **12**, 1916 (2022). https://doi.org/10.3390/nano12111916
30. C. Wu, F. Irshad, M. Luo, Y. Zhao, X. Ma, S. Wang, Ruthenium complexes immobilized on an azolium-based metal-organic framework for highly efficient conversion of CO_2 into formic acid. ChemCatChem **11**, 1256 (2018). https://doi.org/10.1002/cctc.201801701
31. G.I. Dzhardimalieva, R.K. Baimuratova, E.I. Knerelman, G.I. Davydova, S.E. Kudaibergenov, O.V. Kharissova, V.A. Zhinzhilo, I.E. Uflyand, Synthesis of copper(II) trimesinate coordination polymer and its use as a sorbent for organic dyes and a precursor for nanostructured material. Polymers **12**, 1024 (2020). https://doi.org/10.3390/polym12051024
32. S. Wang, X. Xie, W. Xia, J. Cui, S. Zhang, X. Du, Study on the structure activity relationship of the crystal MOF-5 synthesis, thermal stability and N_2 adsorption property. High. Temp. Mater. Proc. **39**, 171 (2020). https://doi.org/10.1515/htmp-2020-0034
33. P. Tshuma, B.C.E. Makhubela, L. Ohrstrom, S.A. Bourne, N. Chatterjee, I.N. Beas, J. Darkwa, G. Mehlana, Cyclometalation of Lanthanum(III) based MOF for catalytic hydrogenation of carbon dioxide to formate. RSC Adv. **10**, 3593 (2020). https://doi.org/10.1039/C9RA09938G
34. M. Köppen, A. Dhakshinamoorthy, K.A. Inge, O. Cheung, J. Ångström, P. Mayer, N. Stock, Metal-organic frameworks as heterogeneous catalysts for the production of fine chemicals. Eur. J. Inorg. Chem. **2018**, 3496 (2018). https://doi.org/10.1039/C3CY00350G
35. F.M.A. Noa, E.S. Grape, M. Åhlen, W.E. Reinholdsson, R.G. Christian, O. Cheung, A.K. Inge, L. Ohrstrom, Chiral lanthanum metal−organic framework with gated CO_2 sorption and concerted framework flexibility. J. Am. Chem. Soc. **144**, 8725 (2022). https://doi.org/10.1021/jacs.2c02351
36. Y. Wang, Y. Miao, S. Li, L. Gao, G. Xiao, Metal-organic frameworks derived bimetallic Cu-Co catalyst for efficient and selective hydrogenation of biomass-derived furfural to furfuryl alcohol. Mol. Catal. **436**, 128 (2017). https://doi.org/10.1016/j.mcat.2017.04.018

37. J. Zhang, D. Wu, Aqueous phase catalytic hydrogenation of furfural to furfuryl alcohol over *in-situ* synthesized Cu–Zn/SiO_2 catalysts. Mater. Chem. Phys. **260**, 124152 (2021). https://doi.org/10.1016/j.matchemphys.2020.124152
38. S.N. Date, A.M. Hengne, K. Huang, R.C. Chikate, C.V. Rode, Single pot selective hydrogenation of furfural to 2-methylfuran over carbon supported iridium catalysts. Green Chem. **20**, 2027 (2018). https://doi.org/10.1039/C8GC00284C
39. A.H. Aboo, E.L. Bennett, M. Deeprose, C.M. Robertson, J.A. Iggo, J. Xiao, Methanol as hydrogen source: transfer hydrogenation of aromatic aldehydes with a rhodacycle. Chem. Commun. **54**, 11805 (2018). https://doi.org/10.1039/C8CC06612D
40. A.W. Gong, C. Chen, H. Wang, H. Zhang, G. Wang, H. Zhao, Sulfonate group modified Ni catalyst for highly efficient liquid-phase selective hydrogenation of bio-derived furfural. Chin. Chem. Lett. **29**, 1617 (2018). https://doi.org/10.1016/j.cclet.2018.03.030
41. R. Fang, L. Chen, Z. Shen, Y. Li, Efficient hydrogenation of furfural to furfuryl alcohol over hierarchical MOF immobilized metal catalysts. Catal. Today **368**, 217 (2020). https://doi.org/10.1016/j.cattod.2020.03.019
42. R. Balaga, P. Balla, X. Zhang, K. Ramineni, H. Du, S. Lingalwar, V. Perupogu, Z.C. Zhang, Enhanced cyclopentanone yield from furfural hydrogenation: promotional effect of surface silanols on Ni-Cu/m-Silica catalyst. Catalysts **13**, 580 (2023). https://doi.org/10.3390/catal13030580
43. K. Yan, A. Chen, Efficient hydrogenation of biomass-derived furfural and levulinic acid on the facilely synthesized noble-metal-free Cu-Cr catalyst. Energy **58**, 357 (2013). https://doi.org/10.1016/j.energy.2013.05.035
44. Y. Wang, J. Huang, S. Lu, P. Li, X. Xia, C. Li, Phosphorus-modified zirconium metal-organic frameworks for catalytic transfer hydrogenation of furfural. New J. Chem. **44**, 20308 (2020). https://doi.org/10.1039/D0NJ04285D
45. F. Zarekarizi, A. Morsali, Dimension control in mixed Iinker metal−organic frameworks *via* adjusting the Iinker shapes. Inorg. Chem. **59**, 2988 (2019). https://doi.org/10.1021/acs.inorgchem.9b03293
46. Y. Jiang, I. Oh, S.H. Joo, Y. Seo, S.H. Lee, W.K. Seong, Y.J. Kim, J. Hwang, S.K. Kwak, J. Yoo, R.S. Ruo, Synthesis of a copper 1,3,5-Triamino-2,4,6-benzenetriol metal−organic framework. J. Am. Chem. Soc. **142**, 18346 (2020). https://doi.org/10.1021/jacs.0c02389
47. Z. Yang, Y. Liu, J. Wang, MOF-derived Cu^0/C activation of molecular oxygen for efficient degradation of sulfamethazine. Chem. Eng. J. **427**, 131961 (2022). https://doi.org/10.1016/j.cej.2021.131961
48. Y. Zhao, X. Wu, J. Zhou, Y. Wang, S. Wang, X. Ma, MOF-derived Cu@C catalyst for the liquid-phase hydrogenation of esters. Catal. Lett. **47**, 883 (2018). https://doi.org/10.1246/cl.180277
49. S. Wang, B. Ye, C. An, J. Wang, Q. Li, Synergistic effects between Cu metal–organic framework (Cu-MOF) and carbon nanomaterials for the catalyzation of the thermal decomposition of ammonium perchlorate (AP). Mater. Sci. **54**, 4928 (2019). https://doi.org/10.1007/s10853-018-03219-4